

Fragmentation in filamentary molecular clouds

Yanett Contreras^{1,2*}, Guido Garay², Jill M. Rathborne¹ and Patricio Sanhueza³

¹*CSIRO Astronomy and Space Science, PO Box 76, Epping NSW 1710, Australia*

²*Departamento de Astronomía, Universidad de Chile, Casilla 36-D, Santiago, Chile*

³*National Astronomical Observatory of Japan, 2-21-1 Osawa, Mitaka, Tokyo 181-8588, Japan*

Accepted 2015 November 26. Received 2015 November 25; in original form 2015 May 15

ABSTRACT

Recent surveys of dust continuum emission at sub-mm wavelengths have shown that filamentary molecular clouds are ubiquitous along the Galactic plane. These structures are inhomogeneous, with over-densities that are sometimes associated with infrared emission and active of star formation. To investigate the connection between filaments and star formation, requires an understanding of the processes that lead to the fragmentation of filaments and a determination of the physical properties of the over-densities (clumps). In this paper, we present a multi-wavelength study of five filamentary molecular clouds, containing several clumps in different evolutionary stages of star formation. We analyse the fragmentation of the filaments and derive the physical properties of their clumps. We find that the clumps in all filaments have a characteristic spacing consistent with the prediction of the ‘sausage’ instability theory, regardless of the complex morphology of the filaments or their evolutionary stage. We also find that most clumps have sufficient mass and density to form high-mass stars, supporting the idea that high-mass stars and clusters form within filaments.

Key words: filamentary molecular cloud — filaments.

1 INTRODUCTION

One striking result of recent dust continuum Galactic Plane surveys is the ubiquitous presence of filamentary structures (e. g., Apex Telescope Large Area Survey (ATLASGAL), Schuller et al. 2009; Bolocam, Nordhaus et al. 2008; Herschel infrared Galactic Plane Survey (HiGAL), Molinari et al. 2010). Their study has recently gained momentum, allowing us to characterize their overall properties and to better understand their formation. (e.g., Teixeira et al. 2005; Myers 2009; André et al. 2010; Arzoumanian et al. 2011; Hernandez & Tan 2011; Myers 2011; Peretto et al. 2012). Filamentary molecular clouds have high aspect ratios (typically larger than 3:1), are often infrared (IR) dark, and harbour over-densities or star-forming clumps along their length.

The processes that form clumps within filamentary molecular clouds are still not well understood. Theoretical work has shown that filaments can be subject to gravitational instabilities, and they should fragment into clumps which are located at a characteristic spacing, given by the wavelength of the fastest growing unstable mode (Chandrasekhar & Fermi 1953; Nagasawa 1987; Inutsuka & Miyama 1992; Nakamura et al. 1993; Tomisaka 1995). Perturbations that are greater than the characteristic wave-

length will become rapidly unstable and clumps (over densities) will be formed within the filament. This preferred spacing depends on the intrinsic characteristics of the filament, the type of fluid (e.g., incompressible, isothermal) and on the shape and strength of any associated magnetic field.

Fiege & Pudritz (2000) modelled the fragmentation of filamentary molecular clouds with a helical magnetic field. They found that filaments that are constrained by these types of magnetic fields are susceptible to both gravitationally driven instabilities and magneto-hydrodynamic (MHD) driven instabilities. One kind of MHD instability that predicts the formation of regularly spaced clumps in a filament is the fluid or ‘sausage’ instability. This mechanism has recently been invoked to explain the regular spacing observed in some filamentary molecular clouds (e.g., Jackson et al. 2010; Miettinen & Harju 2010; Wang et al. 2011).

Once the filament fragments and clumps are formed, some of the clumps will evolve, collapse, and form stars. IR emission associated with some filaments show evidence for heated and shocked gas. Since these are often produced by embedded protostellar objects and are indicators of active star-formation, recent work has proposed that filaments may be important for the process of star formation (e.g. Schisano et al. 2014; Sanhueza et al. 2010). Moreover, some studies have suggested that filaments can also enhance accretion rates on to individual star-forming cores by material

* E-mail: ycontreras@strw.leidenuniv.nl

flowing from the filament to the clumps, and thus potentially facilitating the formation of high mass stars (Banerjee & Pudritz 2008; Myers 2009). To determine whether filamentary molecular clouds and their clumps have the ability to harbour high-mass stars, we have undertaken a detailed study of their global physical properties and their potential to form high-mass stars.

In this paper we characterize the fragmentation within five filamentary clouds and determine the physical properties and star-formation potential of their embedded clumps. The overall properties of these filaments were previously reported by Contreras et al. (2013) (Paper I hereafter, see Table 1).

The five filaments are physically coherent structures in position-position-velocity space, shown via their molecular line emission from the low-density tracer ^{13}CO (3-2). They were selected as contiguous emission features in the ATLASGAL 870 μm dust continuum emission survey and named after their brightest embedded clump using their ATLASGAL catalogue denomination (Contreras et al. 2013). For simplicity, hereafter we refer to each filament with a letter (A through E): ‘A: AGAL337.922-0.456’ (also known as the ‘Nessie Nebula’, Jackson et al. (2010)), ‘B: AGAL337.406-0.402’, ‘C: AGAL335.406-0.402’, ‘D: AGAL332.294-0.094’, and ‘E: AGAL332094-0421’.

The filaments are associated with varying degrees of IR emission identified using the *Spitzer* MIPS Inner Galactic Plane Survey (MIPSGAL; Carey et al. 2009) and in the Galactic Legacy Infrared Midplane Survey Extraordinaire (GLIMPSE; Benjamin et al. 2003) images. Indeed, it is often the case that within a single filament there can be regions that are IR dark, while others can be IR bright and clearly associated with active star formation (see Figures 1-5). Since the presence of IR emission is a signpost of star formation, the varying degree of star formation within these filaments will allow us to also investigate whether or not the separation between clumps change as the clumps evolve.

Moreover, these filaments have a lineal mass (mass per unit length) smaller than their critical mass (virial mass per unit length) suggesting that they are supported by an helical toroidal dominated magnetic field (Paper I). Thus, MHD driven instabilities, such as the ‘sausage’ instability, may be responsible for the formation of the clumps within these filaments.

Section 2 describes the dust continuum and molecular line observations made towards the filaments. Section 3 summarizes the physical properties of the embedded clumps. In Section 4 we discuss the star formation activity within the clumps determined from their IR and molecular line emission. In Section 5 we analyse the fragmentation of the filaments and discuss the potential of the clumps to form high-mass stars.

2 THE DATA

2.1 ATLASGAL: 870 μm dust continuum emission

We used the ATLASGAL (Schuller et al. 2009) maps to measure the dust thermal emission at 870 μm towards each filament. The ATLASGAL survey was carried out using the Large Apex Bolometer Camera (LABOCA) bolometer receiver (Siringo et al. 2009) mounted at Atacama Pathfinder

EXperiment (APEX; Güsten et al. 2006), located in the Llano de Chajnantor, Chile. At this frequency the APEX beam size is $19''.2$. The uncertainty in flux is estimated to be lower than 15% (Schuller et al. 2009) and the pointing rms is $\sim 4''$. The 1σ noise of the data is typically 50 mJy beam^{-1} .

2.2 MALT90: 90 GHz dense gas emission

We use data from the Millimetre Astronomy Legacy Team 90 GHz survey (MALT90; Foster et al. 2013; Jackson et al. 2013) to determine the dynamical state of the clumps and to derive the properties of the dense gas within the clumps. The MALT90 survey covered 80 of the 101 clumps within these filaments. Hereafter, we will refer to these clumps as MALT90 clumps.

The MALT90 survey was conducted using the 8 GHz wide Mopra Spectrometer (MOPS) at the Mopra 22-m radio telescope, simultaneously mapping 16 spectral lines near 90 GHz (Table 2). The maps have an angular and spectral resolution of $38''$ and 0.11 km s^{-1} , respectively. The typical 1σ noise in the spectra is $T_A^* \sim 0.2\text{ K}$ per channel. The pointing is accurate to $8''$ and the system gain is repeatable to within 30% (Foster et al. 2013). The maps were reduced by the MALT90 team using an automated reduction pipeline. The reduced and calibrated data products are available to the community via Australian Telescope Online Archive, ATOA¹.

The transitions observed in this survey offer an excellent combination of optically thin and thick tracers and cover a broad range in critical densities and excitation temperatures. Table 2 summarises the lines included within the survey and their properties (excitation energy and critical density). For simplicity throughout the paper we will refer to each transition only by their molecular name, i.e., HCO^+ instead of $\text{HCO}^+(1-0)$.

For each MALT90 clump we extract the line parameters determined via Gaussian profile fitting to the spectra reported in the MALT90 catalog (Rathborne et al, in prep) (velocity, v_{LSR} ; line width, Δv ; and peak antenna temperature, T_A^*). Table 3 shows an example of some of the MALT90 data for the clumps embedded in filament A, the rest of the MALT90 data is available as an online table.

3 PROPERTIES OF THE EMBEDDED CLUMPS

3.1 Identification of the clumps

The 870 μm continuum emission was used to pinpoint the location of the clumps along each filament. Since this emission traces well both the IR bright and dark regions, it provides an homogenous method to determine the position of the clumps. The clumps were identified by searching the ATLASGAL compact source catalogue for all the clumps located within the more extended 870 μm continuum emission that defined each filament (see Paper I, for further details). We found a total of 101 clumps within these five filaments.

¹ <http://atoa.atnf.csiro.au/malt90>

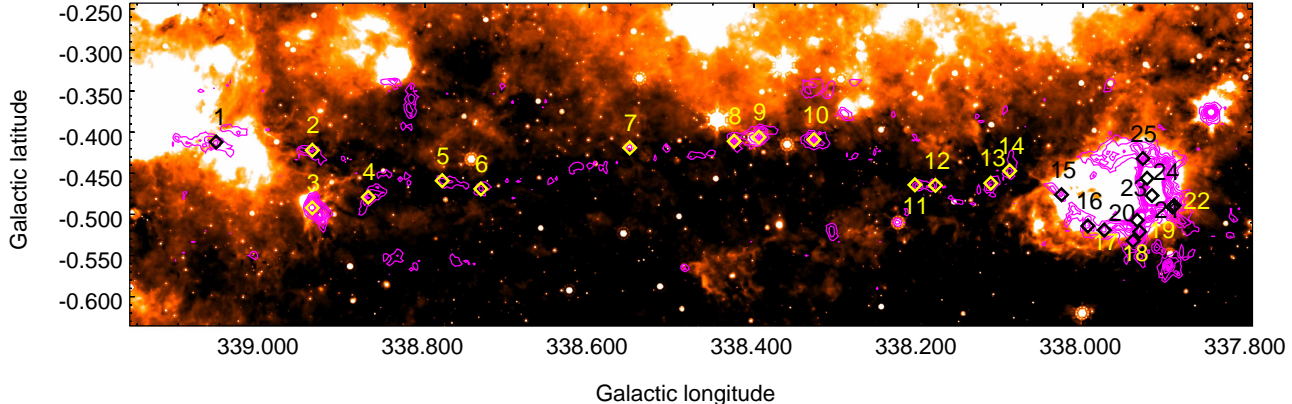


Figure 1. $24\ \mu\text{m}$ *Spitzer*/MIPS image toward filament A: AGAL337.922-0.456, ‘Nessie’ (Jackson et al. 2010). The $870\ \mu\text{m}$ ATLASGAL emission is overlaid as contours (2 to $10\ \sigma$). Black and yellow diamonds indicate the position of the clumps, identified from the ATLASGAL compact catalog (Contreras et al. 2013). The numbers correspond to the ID given to the clumps. For clarity, we have removed the letter in each clump. While most of the clumps have little infrared emission, some show star formation indicators such as compact 8 and $24\ \mu\text{m}$ emission.

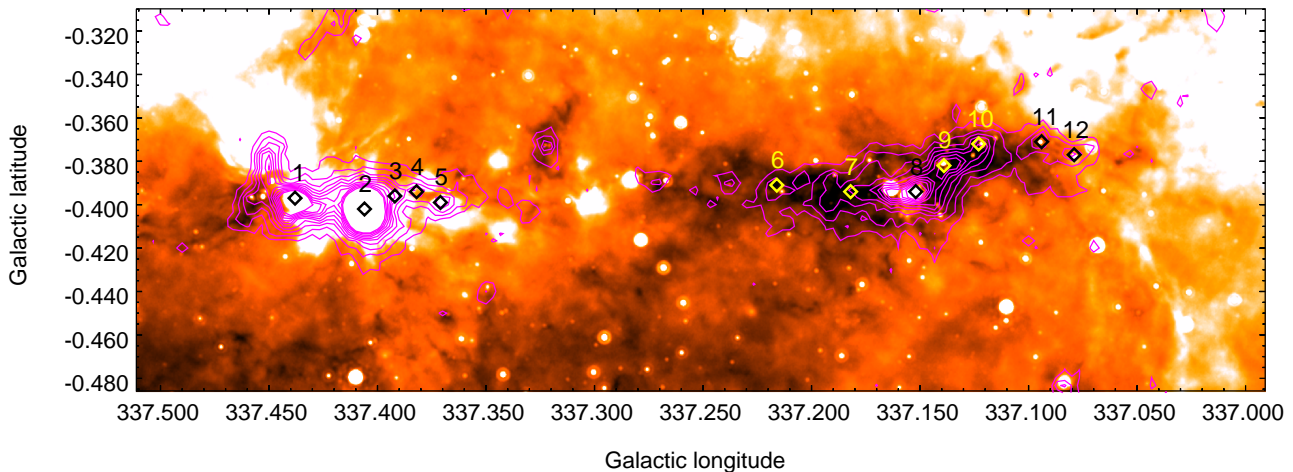


Figure 2. $24\ \mu\text{m}$ *Spitzer*/MIPS image toward filament B: AGAL337.406-0.402. Contours and symbols as in Figure 1. This filament contains both infrared-dark and infrared-bright clumps.

Table 4 lists for each clump its abbreviated ID and its full ATLASGAL denomination.

3.2 Clump sizes, masses, and volume densities

The size, mass, and volume density of the clumps were derived from the observed molecular line and dust continuum emission. The size of a clump was defined as twice the effective radius listed in the ATLASGAL compact source catalogue (Contreras et al. 2013). Using the kinematic distance to each filament (from Paper I, listed in Table 1), we obtained the physical size for each clump. The sizes range between 0.26 and 1.6 pc, with an average of ~ 0.5 pc (see Table 4). The masses of the clumps, derived from their dust con-

tinuum emission, were determined using the relation (Hildebrand 1983),

$$M_{dust} = \frac{S_{870} D^2 R_{gd}}{\kappa_{870} B_{870}(T_d)}, \quad (1)$$

where S_{870} is the flux density at $870\ \mu\text{m}$, obtained from the ATLASGAL compact source catalog, D is the kinematic distance to the source, R_{gd} is the gas to dust mass ratio assumed as 100 , κ_{870} is the dust absorption coefficient, B_{870} is the Planck function at $870\ \mu\text{m}$ and T_d is the dust temperature. We assumed a dust temperature based on the observed degrees of IR emission (see section 4.1) and assumed $\kappa_{870} = 1.85\ \text{cm}^2\ \text{gr}^{-1}$, interpolated from Ossenkopf & Henning (1994). With these assumptions we calculated the clump masses and found that they range from ~ 20 to

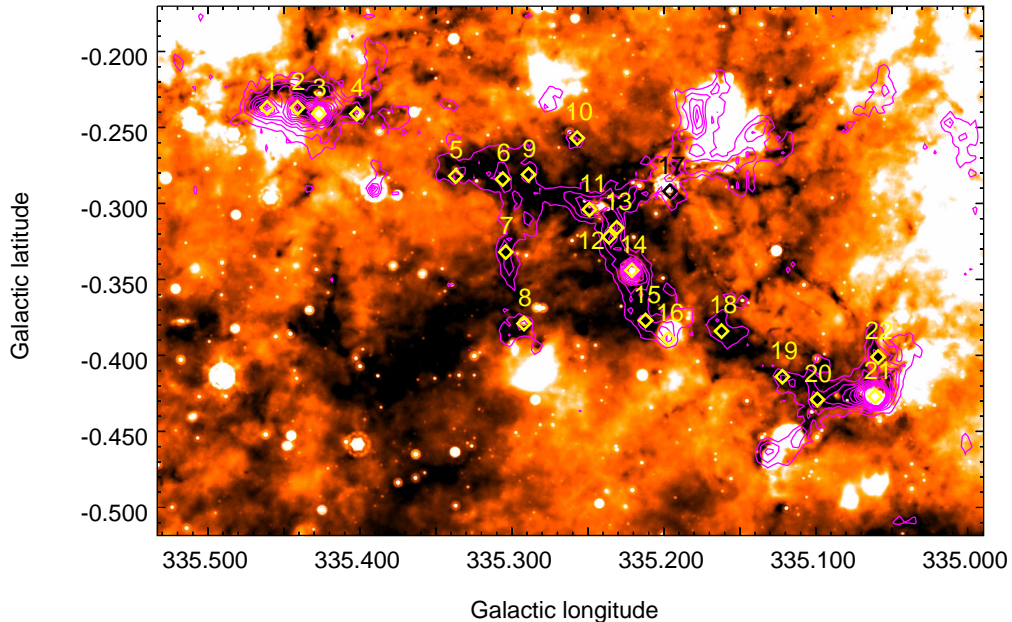


Figure 3. $24\ \mu\text{m}$ *Spitzer*/MIPS image toward filament C: AGAL335.406-0.402. Contours and symbols as in Figure 1. This filament represents a good example of the hub-tail structure described in Myers (2011), showing a main body that run from clump 1 to clump 21 and several ramifications. This filament is also in a young evolutionary stage with many clumps appearing dark in GLIMPSE/MIPSGAL.

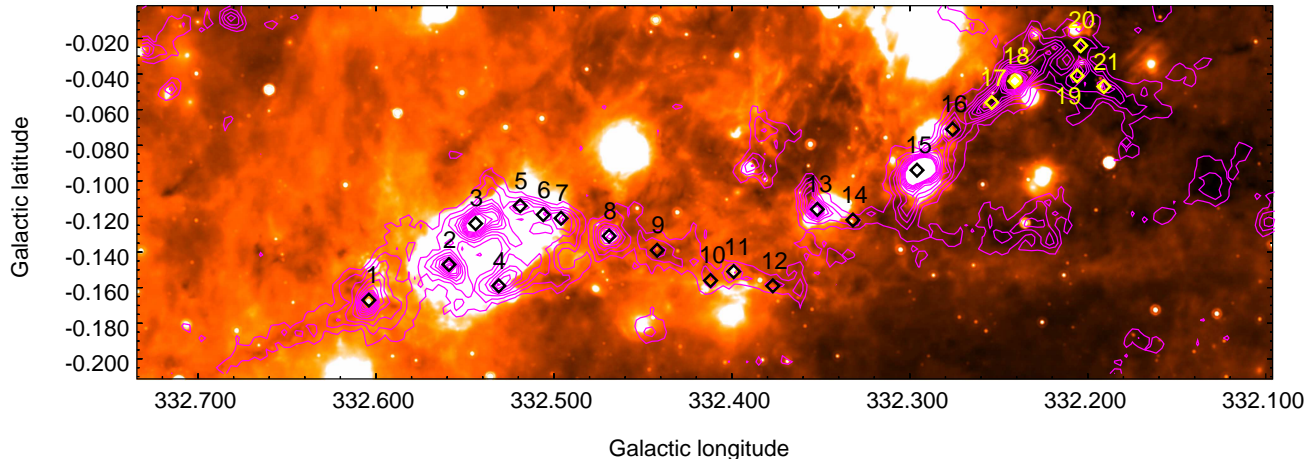


Figure 4. $24\ \mu\text{m}$ *Spitzer*/MIPS image toward filament D: AGAL332.294-0.094. Contours and symbols as in Figure 1. This filament is an example of a more evolved structure with several clumps associated with bright infrared emission. Here, we can see that around the HII region clumps (bright region in this image) the clumps are closer, while the rest of the filament the clumps remain more evenly spaced.

$2500\ M_{\odot}$ (see Table 4). Assuming the clumps have roughly spherical shapes, we compute the H_2 volume density via $n(\text{H}_2) = 3M_{\text{dust}}/4\pi r^3$, finding values ranging from 10^3 to $10^5\ \text{cm}^{-3}$ (see Table 4).

The virial mass was calculated using the size of the clumps and the line width derived from the N_2H^+ (1-0) emission. The optical depth of the N_2H^+ (1-0) emission is usually $\lesssim 1$, thus, this molecular line is suitable for determining the

virial parameter (e.g. Sanhueza et al. 2012). Optically thick lines would overestimate the virial mass. We found a total of 71 clumps for which there are MALT90 detections of N_2H^+ . For these clumps, we use the line width obtained from the hyperfine structure fitting to compute their virial mass. The virial mass of a clump of radius r and line-width Δv is given by,

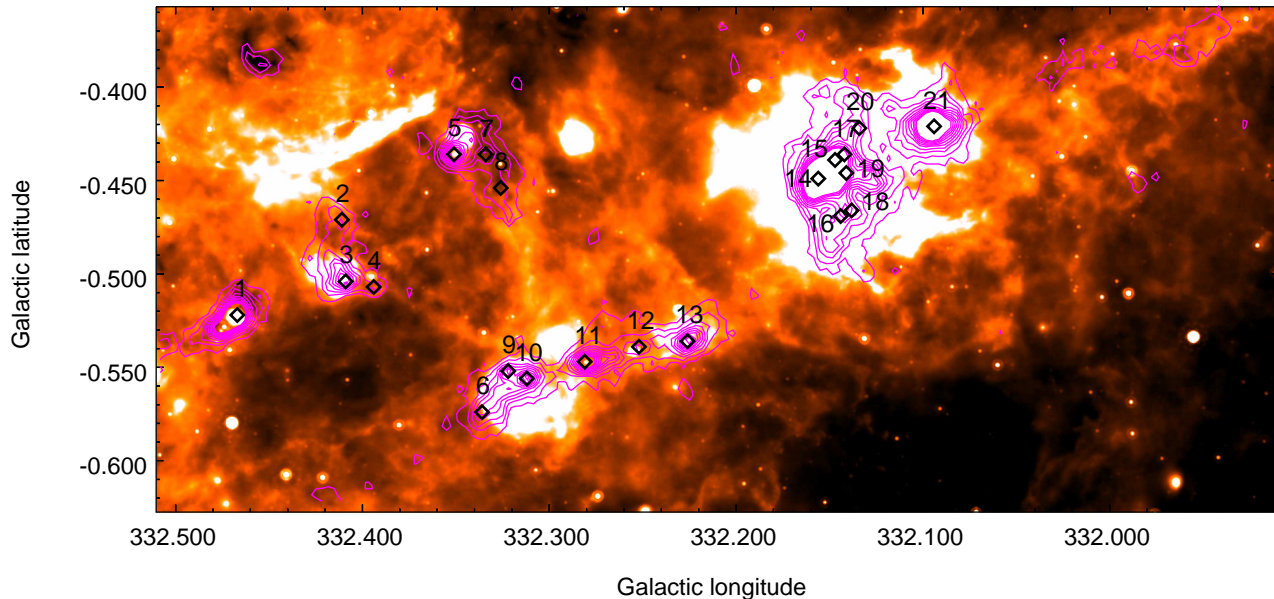


Figure 5. $24\ \mu\text{m}$ *Spitzer*/MIPS image toward filament E: AGAL332.094-0.421. Contours and symbols as in Figure 1. This image shows a small filament composed by 6 clumps (clumps 8-13) associated with bright infrared emission. This is an example of a more evolved filament with all of its clumps showing signs of active star formation.

$$M_{vir} = \frac{5r\Delta v^2}{8\ln(2)a_1a_2G} \sim 209 \frac{1}{a_1a_2} \left(\frac{\Delta v}{\text{km s}^{-1}} \right)^2 \left(\frac{r}{pc} \right) M_{\odot}, \quad (2)$$

where a_1 is the correction for a power-law distribution given by $a_1 = \frac{1-p/3}{1-2p/5}$, $p < 2.5$, and a_2 is the correction for a non spherical shape (Bertoldi & McKee 1992). To calculate a_1 we use a power law density distribution of $p = 1.8$. We assume that the clumps in our sample have spherical shapes, therefore we used $a_2 = 1$ for all clumps. With these assumptions, we found that the clumps have virial masses ranging from ~ 50 to $\sim 1700 M_{\odot}$ (see Table 4).

4 EVIDENCE FOR STAR FORMATION WITHIN THE CLUMPS

4.1 Infrared signatures of star formation

To characterize the star formation activity within each clump, we used *Spitzer* $24\ \mu\text{m}$ MIPS GAL and $3.6 - 8\ \mu\text{m}$ GLIMPSE surveys.

Using these IR images we classified the clumps into four broad categories: ‘pre-stellar’ clumps, appearing dark at $3.6-8\ \mu\text{m}$, and $24\ \mu\text{m}$; ‘proto-stellar’ clumps, having a $24\ \mu\text{m}$ point like emission that traces the dust heated by embedded proto-stars, or enhancement in the emission at $4.5\ \mu\text{m}$, indicative of the presence of shocked gas (**often referred too in the literature as extended green objects, or ‘green fuzzies’, for their green appearance in a composite image where green is used to represent $4.5\ \mu\text{m}$ emission**); ‘HII region’ clumps, associated with bright, compact 8 and $24\ \mu\text{m}$ emission; and ‘PDRs clumps’ showing

extended and often diffuse 8 and $24\ \mu\text{m}$ emission. These categories broadly describe the evolution of a clump since the IR emission associated within a clump will increase as their embedded stars form and heat their immediate surroundings. (Chambers et al. 2009; Jackson et al. 2013). Using this scheme we categorized 31 of the clumps as ‘pre-stellar’ (30%), 30 as ‘proto-stellar’ (30%), 11 as ‘HII region’ clumps (11%), and 29 as PDRs (29%).

For each clump we assumed a dust temperature equal to the average temperature of its classification obtained by Guzman et al. (in press.) for a large sample of clumps located in the Galactic plane. Guzman et al. derived dust temperatures for all MALT90 clumps, by fitting their dust continuum emission using data from the Hi-GAL and ATLASGAL surveys. The average dust temperatures are 17 K for ‘pre-stellar’ clumps, 19 K for ‘proto-stellar’ clumps, 24 K for clumps associated with ‘HII regions’, and 28 K for PDRs. Since, not all the clumps detected in the filaments have MALT90 observations, in this paper we use the average dust temperature derived for the relevant category in calculations for each of the individual clumps. Table 4 summarizes the properties of the IR emission detected towards each clump as well as their IR-based classification and assumed dust temperature.

We found that the amount of IR emission and the number of clumps assigned to each category differed between the filaments, suggesting that the filament span a range of evolutionary stages. In filaments A and C, most of the clumps are IR dark. In filament B, some of the clumps are dark and others are IR bright. In filaments D and E, most of the clumps are associated with ‘HII regions’ and PDRs.

	Dense, Low E_u/k					Isotopologues			Shocks	Dense, High E_u/k		
PDRs	100	91	91	91	68	45	18	14	9	27	0	0
HII Region	100	90	90	80	80	70	30	20	20	30	0	0
Proto-stellar	100	92	52	60	28	48	40	4	8	8	4	4
Pre-stellar	100	83	57	65	30	9	9	4	0	9	0	0
	HNC	N_2H^+	HCN	HCO^+	C_2H	$H^{13}CO^+$	$HN^{13}C$	^{13}CS	SiO	HC_3N	HNCO	CH_3CN

Figure 6. Detection rate of the MALT90 clumps. Numbers indicate the percentage of clumps for which each molecule was detected.

4.2 Molecular line signatures of star formation

4.2.1 Detection rates and evolutionary stage

An embedded proto-star influences the gas chemistry of its immediate surrounding as it forms and evolves. In the initial stages, a clump’s interior will have low temperatures and high density, where molecules are stuck on the icy dust grains. As a proto-star evolves and starts heating its surrounding environment, molecules will be released into the gas phase and their emission will be detected.

MALT90 observations were used to determine the molecular line detection rates towards the clumps and their relationship with their star formation activity. Figure 6 summarizes the detection rates for each molecule for the MALT90 clumps broken into their IR-based categories. We found that the number of molecular species detected increases from the clumps classified as ‘pre-stellar’ to the clumps associated with ‘HII Regions’ and PDRs, which reflects the increased complexity in the chemistry as the embedded proto-stars within these clumps form and evolve.

Of the four main dense gas tracers, emission was detected in HNC (above 3σ) towards all 80 MALT90 clumps, in N_2H^+ towards 89%, in HCO^+ towards 73% and in HCN towards 69% of the MALT90 clumps. These molecules are typical tracers of high density gas and are detected over a broad range of gas temperatures and evolutionary stages (e.g., Sanhueza et al. 2012; Hoq et al. 2013). We find that, in general, the morphology of the N_2H^+ emission traces very well the clumps, while the HNC emission is more extended tracing well the overall morphology of the filaments.

The reactive radical ethynyl (C_2H) has been detected in quite different environments such as those towards low-mass cores (Millar & Freeman 1984), PDRs (Jansen et al. 1995), high-mass star forming regions (Beuther et al. 2008) and infrared dark clouds (Sanhueza et al. 2012, 2013). For the MALT90 clumps, C_2H was detected toward 30% of the ‘pre-stellar’ clumps, 28% of the ‘proto-stellar’ clumps, 80% of the ‘HII region’ clumps and in 68% of the PDRs. We find that the morphology of the C_2H emission matched well the morphology of the HNC and N_2H^+ emission towards the ‘pre-stellar’ and ‘proto-stellar’ clumps. In contrast, however, the C_2H emission associated with the PDR clumps appears to

more closely follow the extended, diffuse background emission.

Emission from the isotopologues $HN^{13}C$, $H^{13}CO^+$ and ^{13}CS was detected predominantly towards the ‘proto-stellar’ clumps and ‘HII region’ clumps, $H^{13}CO^+$ being the most frequently detected isotopologue. SiO was detected toward six clumps: two ‘proto-stellar’, two ‘HII region’ clumps, and two PDRs. SiO is usually associated with outflows, because the Si atoms are released from dust into the gas phase by shocks produced by outflows from newly formed stars. Since the presence of enhanced $4.5 \mu m$ emission (relative to 3 and $8 \mu m$) may also arise from shocked gas, one might expect a tight correlation between those clumps with extended $4.5 \mu m$ emission and the presence of SiO. We found that about 10% of the $4.5 \mu m$ bright clumps have detected SiO emission. This low detection rate of SiO towards these clumps may reflect the MALT90 sensitivity limit, the differences in the angular resolution of the two data sets (the MALT90 data will be significantly beam diluted), or it may indicate that the proto-stars in these clumps are in an early evolutionary stage, and they have not yet evolved to produce outflows that sufficiently excite the SiO.

Less frequently detected was the emission from ‘hot core chemistry’ molecules such as HC_3N (16%), CH_3CN (4%) and HNCO(4%). HC_3N was detected in 9% of the ‘pre-stellar’ clumps, 8% of the ‘proto-stellar’ clumps, 30% of the ‘HII region’ clumps and 27% of the PDRs. As expected, we find that the detection rate for these more complex molecules increases towards the more evolved clumps. CH_3CN and HNCO were only detected towards four clumps, all of these clumps were classified as ‘proto-stellar’. No emission was detected in the HNCO ($J_{K_a, K_b} = 4_{1,3}-3_{1,2}$), $HC^{13}CCN$, $^{13}C^{34}S$ and H41 α lines toward any of the 80 MALT90 clumps.

5 DISCUSSION

5.1 The fragmentation of filaments via the ‘sausage’ instability

The process leading to the formation of clumps in filaments is yet to be understood, but theoretical work shows that fil-

Table 1. Summary of the relevant properties of the filaments used in this work. For more details refer to Paper I on the values of the distance (D), Radius of the filament (r), line width (Δv), central density (ρ_c), inner flat region radius (R_{flat}) and the index of the intensity profile that relates to the magnetic field support (p). NC is the number of clumps detected in each filament. λ_{obs} is the observed spacing between the clumps in each filament, with the error give by the standard deviation between the separation between consecutive clumps and the average observed separation. $H_{eff,0}$ and $\lambda_{s,0}$ correspond to the non magnetic solution, i.e. $\gamma = 0$. B_c is the value of the magnetic field that produce a $\lambda_s = \lambda_{obs}$.

Filament	D	r	NC	Δv	ρ_c	R_{flat}	p	$H_{eff,0}$	λ_{obs}	$\lambda_{s,0}$	B_c
	(kpc)	(pc)		(km s ⁻¹)	$\times 10^{-19}$ (gr cm ⁻³)	(pc)		(pc)	(pc)	(pc)	(μG)
A	3.0	0.44	25	^a 2.8	0.74	0.25	3.0	0.155	3.2 ± 2.4	3.4	110
B	3.2	0.45	12	2.4	1.7	0.30	2.0	0.091	1.9 ± 2.1	2.0	128
B1	3.2	0.45	5	2.4	1.7	0.30	2.0	0.091	1.3 ± 0.4	2.0	537
B2	3.2	0.45	7	2.4	1.7	0.30	2.0	0.091	1.0 ± 0.5	2.0	1031
C	3.6	0.56	22	2.7	1.2	0.64	3.1	0.116	2.4 ± 1.7	2.6	133
D	3.3	0.52	21	2.1	1.3	0.58	2.0	0.086	1.7 ± 0.7	1.9	151
E	3.7	0.23	21	3.3	3.0	0.50	2.6	0.091	1.6 ± 0.5	2.0	580

^a We used here the mean value of the N₂H⁺ emission, since the ¹³CO(3-2) observations toward this filament don't cover their full extent (see Paper I for more details).

aments can fragment due to gravitational and MHD driven instabilities (Fiege & Pudritz 2000; Chandrasekhar & Fermi 1953; Nagasawa 1987; Inutsuka & Miyama 1992; Nakamura et al. 1993; Tomisaka 1995). Because the selected filaments are consistent with being confined by a helicoidal, toroidal-dominated magnetic field (see Paper I), we consider the fragmentation of these filaments in the framework of the MHD instabilities within filaments that are also confined by such magnetic fields. In particular, our goal is to determine whether or not the ‘sausage’ MHD instability is able to accurately describe the observed spacing between the clumps within each of the filaments.

The selected filaments can be represented by an isothermal finite cylinder with an helicoidal magnetic field. In this case, Nakamura et al. (1993) predicted a preferred spacing given by,

$$\lambda_s = 8.73H[(1 + \gamma)^{1/3} - 0.6]^{-1}, \quad (3)$$

where $\gamma = B_c^2/(8\pi\rho_c c_s^2)$, c_s is the sound speed, B_c is the magnetic field strength, ρ_c is the central density of the filament, and H is the scale of height, given by,

$$H = c_s(4\pi G\rho_c)^{-1/2}[1 + \gamma/4]^{1/2}, \quad (4)$$

where G is the gravitational constant. Thus, when magnetic fields are considered, the expected spacing between the clumps is predicted to be smaller than the pure non-magnetic case.

Because the observed line-widths of the molecular tracers detected towards these filaments show that the turbulent pressure dominates over the thermal pressure, the sound speed c_s in Equation 4 should be replaced by the velocity dispersion σ (Fiege & Pudritz 2000) of the gas in the filament, hence:

$$H_{eff} = \sigma(4\pi G\rho_c)^{-1/2}[1 + \gamma/4]^{1/2}, \quad (5)$$

where $\gamma = B_c^2/(8\pi\rho_c\sigma^2)$. If $\gamma = 0$, thus $\lambda_{s,0} = 21.8H_{eff,0}$ with $H_{eff,0} = \sigma(4\pi G\rho_c)^{-1/2}$.

The central densities of the filaments were estimated

from the fit to the 870 μm dust continuum emission, as described in Paper I assuming an intensity profile given by (Arzoumanian et al. 2011),

$$I(r) = A_p \frac{\rho_c R_{flat}}{[1 + (r/R_{flat})^2]^{p/2}} \frac{k_\lambda B_\lambda(T_{dust})}{d^2}, \quad (6)$$

where $I(r)$ is the dust continuum emission intensity profile; p is an index that gives an indirect measurement of the magnetic field support over the filament (in the non-magnetic case $p = 4$; Ostriker (1964); and $p < 3$ if the filament is magnetically supported, Fiege & Pudritz (2000)); A_p is a constant given by $A_p = \int_0^\infty du/(1 + u^2)^{p/2}$ for $p > 1$, which is equal to $\pi/2$ for the non-magnetic case; R_{flat} is the radius of an inner flat region, which in the non-magnetic case corresponds to the thermal Jeans length at the centre of the filament; k_λ is the dust opacity; B_λ is the Planck function; T_{dust} is the average dust temperature of the filament, assumed to be 20 K; and d is the distance to the filament. The values of ρ_c , R_{flat} , p , and $H_{eff,0}$ for these filaments are summarized in Table 1.

Using the ATLASGAL maps we measured the separation between a clump and its nearest neighbour clump. Because the velocity gradient in the filaments is small, we assume that the filaments are perpendicular to the line of sight when calculating the observed spacing.

The average value of the observed spacings, λ_{obs} , between the clumps range from 1.0 to 3.2 (see Table 1). To measure how periodic is the location of the clump within the filament, the error in the observed spacing was calculated by taking the standard deviation between the separation of consecutive clumps and the average observed spacing. Filament B has weak dust 870 μm dust continuum emission towards its centre, creating two sections within this filament. If we treat each section independently (B1 and B2, in Table 1), then the clump observed spacing in each section is more periodic (the associated error in each section is smaller).

The theoretical spacing predicted for each filament assuming $\gamma = 0$, $\lambda_{s,0}$, range between 1.9 and 3.4 pc (see Ta-

ble 1). In general $\lambda_{s,0}$ is slightly higher than the observed spacings in all the filaments. This discrepancy could be attributed to the presence of magnetic fields. We find that to explain the observed spacing, the ‘sausage’ instability theory requires magnetic fields ranging between ~ 110 and $580 \mu\text{G}$.

Regardless of their complex morphology or evolutionary stage, we found that for all filaments the predicted spacing given by the ‘sausage’ instability theory and the observed spacing matches well for the case of a helical magnetic field with strength of hundreds μG . This suggests that this mechanism could work not only for ‘ideal’ filaments such as ‘Nessie’ but also for filaments that have more complex morphologies. The average spacing of the more evolved filaments is also similar to the predicted initial spacing given by this theory. This would imply then, that if the clumps are formed via this mechanism, as they evolve into HII regions and PDRs and disrupt their environment, the average spacing along the whole filament is not significantly affected over time. This means that we can trace the fragmentation of the filaments, even if they are evolved, by observing their sub-millimetre continuum emission.

5.2 Star formation within the filaments

From the observed IR emission detected towards the clumps, we were able to estimate the overall star formation activity within the filaments. Filaments A, B and C have a higher number of clumps in the ‘pre-stellar’ phase, while filaments E and D contain a relatively higher number of clumps in more evolved evolutionary stages (i.e., ‘HII region’ clumps and PDRs). In this section we discuss the virial state of the clumps embedded and their potential to form high-mass stars.

5.2.1 Are the clumps gravitationally bound?

To determine whether the clumps are gravitationally bound, we calculated the virial parameter α (ratio between the virial and dust mass) for those clumps with molecular line information. The parameter α is commonly used to determine if a clump is stable against collapse. If $\alpha > 1$ the clump contains enough kinetic energy to expand unless it is confined by an external mechanism. A value of $\alpha < 1$ indicates that the kinetic energy is not enough to support the clump against gravitational collapse (Kauffmann et al. 2013).

We find that 83% of MALT90 clumps have values of $\alpha \leq 1$ and are unstable to gravitational collapse, if magnetic fields are ignored. Figure 7 shows the values of the virial parameter for all the clumps colour coded by their IR-based categories. Most of the ‘pre-stellar’ and ‘proto-stellar’ clumps have virial parameter with values < 1 , suggesting that there are gravitationally bound and likely to collapse. This is supported with the fact that ‘proto-stellar’ clumps are currently forming stars, and thus are likely collapsing. Only one ‘pre-stellar’ clump and two ‘proto-stellar’ clumps have values of $\alpha \geq 1$, thus, they might correspond to transient clumps. We find that all the ‘HII region’ clumps also have ‘virial parameter’ lower than 1, suggesting that their recently formed proto-star has not yet significantly affected the clump dynamics. The PDRs have virial parameters that

have a wider range in values, which is also expected for these late evolutionary stages where the expansion of the clumps is expected due to the UV radiation and stellar winds from the newly formed high-mass stars.

5.2.2 Will the clumps form high-mass stars?

The total mass of the clumps in each filament, are 1.3×10^4 , 1.1×10^4 , 1.5×10^4 , 1.3×10^4 and $6.2 \times 10^3 M_{\odot}$ for filaments A, B, C, D and E respectively. To determine the potential of these clumps to form high-mass stars ($> 8 M_{\odot}$), we conservatively assumed that 30% of the mass of the clumps will form cores, and that only 10% of the mass in the cores will eventually be converted into stars. Given a typical initial mass function (IMF; e.g. Salpeter 1955), we determined that all the filaments will have enough material to form more than one star with a mass $> 8 M_{\odot}$.

While it appears that the clumps have sufficient mass to form at least one high-mass star, we must also consider their sizes and volume densities. Figure 8 shows the mass versus radius plot for all the 101 clumps embedded in the five filaments. We compare the mass and sizes of our clumps with the limits established by Kauffmann et al. (2010) for clumps devoid of high-mass star formation, which follow the relationship $M(r) \leq 870 M_{\odot} (r/\text{pc})^{1.33}$. We find that 98% of the clumps lie above the threshold for clump devoid of high-mass stars. This provide additional support to the idea that these clumps will harbour high-mass stars.

6 SUMMARY

Using data from the ATLASGAL, *Spitzer*, and MALT90 surveys we characterized the physical properties, chemistry, kinematics, and star formation activity of 101 clumps embedded in five filamentary molecular clouds. We find that each filament harbour several clumps, covering a wide range of masses from hundred to thousands solar masses.

We studied the emission of dense gas tracers towards 80 clumps using MALT90 data. We find that the number of lines detected towards the clumps increases with the amount of associated IR emission and, hence, active star formation. Emission in the HNC line was detected towards all 80 clumps. N_2H^+ , HCO^+ , HCN and C_2H were detected toward 89%, 73%, 69% and 46% of the clumps, respectively. For clumps with classified as ‘pre-stellar’ and ‘proto-stellar’, the morphology of the C_2H emission is similar to that of the dust emission and other molecules. For clumps classified as PDR, C_2H traced well the morphology observed in the PDRs. The isotopologues HN^{13}C , H^{13}CO^+ , and ^{13}CS were detected more frequently towards ‘proto-stellar’ clumps, ‘HII region’ clumps and PDRs than ‘pre-stellar’ clumps. SiO emission was detected towards $\sim 10\%$ of the MALT90 clumps and less frequently detected was emission from the “hot core chemistry” molecules.

Assuming that the filaments are isothermal finite cylinders supported by a helicoidal magnetic field, we find that the observed separation of the clumps can be explained via the ‘sausage’ instability theory for magnetic field in the range from ~ 110 to $580 \mu\text{G}$. Moreover, we found that regardless of the morphology and evolutionary stage exhibited by

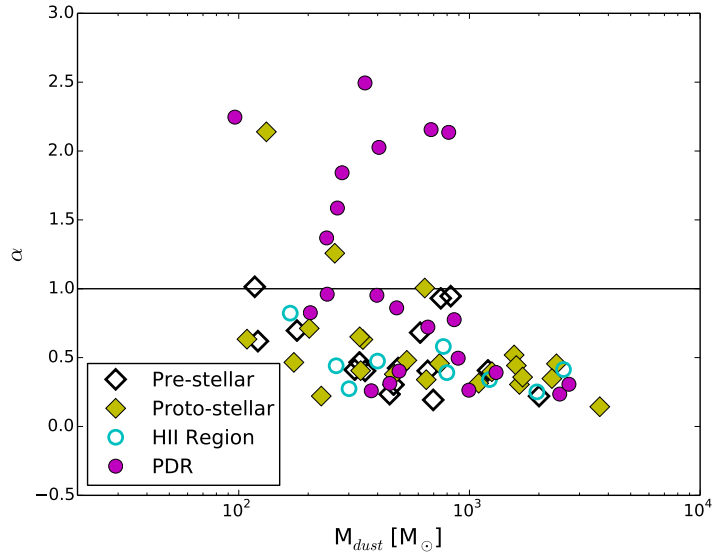


Figure 7. Virial parameter for the clumps in each evolutionary stage. Most of the ‘pre-stellar’ and ‘proto-stellar’ clumps have values of $\alpha < 1$, suggesting that they are gravitationally bound and likely to form stars. PDRs have a wider range in values consistent with this late evolutionary stage where clumps are expected to expand.

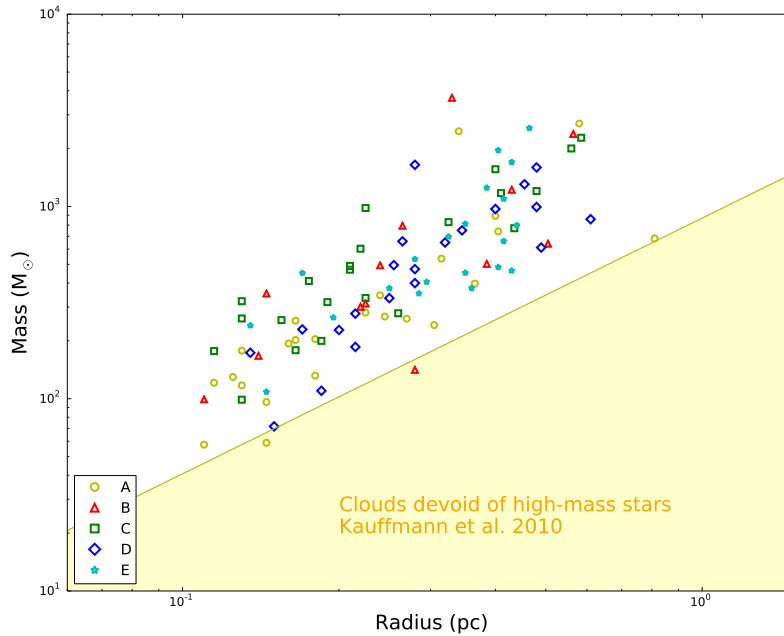


Figure 8. Mass versus radius for the clumps embedded in the filaments. The clumps for different filaments are shown in different colours and symbols. The legend shows the colours and symbols used for each filament. The yellow region shows the parameter space for clumps devoid of high-mass stars. All but 2 of our clumps lie above the region of clumps devoid of high-mass stars, suggesting that all the filaments will harbour high-mass stars.

the filaments, by following the dust continuum emission we can still trace the underlying structure within the filament.

The derived virial parameter for the clumps reveals that they are typically gravitationally bound. Given the clump masses and assuming a typical IMF, we found that every filament host a clump that is likely to form at least one high-mass star. We also analysed the mass versus radius relationship of the clumps, finding that most of the clumps are likely to form high-mass stars. This result further supports the idea that filaments are the birthplaces of high-mass stars and their associated clusters.

ACKNOWLEDGMENTS

We thank the referee Michael Burton for his valuable comments that significantly improved this paper. YC and GG gratefully acknowledge support from CONICYT through projects FONDAF No. 15010003 and BASAL PFB-06.

REFERENCES

- André P. et al., 2010, *A&A*, 518, L102
 Arzoumanian D. et al., 2011, *A&A*, 529, L6+
 Banerjee R., Pudritz R. E., 2008, in H. Beuther, H. Linz, & T. Henning ed., *Astronomical Society of the Pacific Conference Series Vol. 387, Massive Star Formation: Observations Confront Theory*. p. 216
 Benjamin R. A. et al., 2003, *PASP*, 115, 953
 Bertoldi F., McKee C. F., 1992, *ApJ*, 395, 140
 Beuther H., Semenov D., Henning T., Linz H., 2008, *ApJ*, 675, L33
 Carey S. J. et al., 2009, *PASP*, 121, 76
 Chambers E. T., Jackson J. M., Rathborne J. M., Simon R., 2009, *ApJS*, 181, 360
 Chandrasekhar S., Fermi E., 1953, *ApJ*, 118, 116
 Contreras Y., Rathborne J., Garay G., 2013, *MNRAS*, 433, 251
 Contreras Y. et al., 2013, *A&A*, 549, A45
 Fiege J. D., Pudritz R. E., 2000, *MNRAS*, 311, 85
 Foster J. B. et al., 2013, *PASA*, 30, 38
 Güsten R. et al., 2006, in *Ground-based and Airborne Telescopes*. Edited by Stepp, Larry M. *Proceedings of the SPIE, Volume 6267*, pp. 626714 (2006)..
 Hernandez A. K., Tan J. C., 2011, *ApJ*, 730, 44
 Hildebrand R. H., 1983, *QJRAS*, 24, 267
 Hoq S. et al., 2013, *ApJ*, 777, 157
 Inutsuka S.-I., Miyama S. M., 1992, *ApJ*, 388, 392
 Jackson J. M., Finn S. C., Chambers E. T., Rathborne J. M., Simon R., 2010, *ApJ*, 719, L185
 Jackson J. M. et al., 2013, *PASA*, 30, 57
 Jansen D. J., van Dishoeck E. F., Black J. H., Spaans M., Sosin C., 1995, *A&A*, 302, 223
 Kauffmann J., Pillai T., Goldsmith P. F., 2013, *ApJ*, 779, 185
 Kauffmann J., Pillai T., Shetty R., Myers P. C., Goodman A. A., 2010, *ApJ*, 716, 433
 Miettinen O., Harju J., 2010, *A&A*, 520, A102
 Millar T. J., Freeman A., 1984, *MNRAS*, 207, 405
 Molinari S. et al., 2010, *PASP*, 122, 314
 Myers P. C., 2009, *ApJ*, 700, 1609
 Myers P. C., 2011, *ApJ*, 735, 82
 Nagasawa M., 1987, *Progress of Theoretical Physics*, 77, 635
 Nakamura F., Hanawa T., Nakano T., 1993, *PASJ*, 45, 551
 Nordhaus M. K. et al., 2008, in A. Frebel, J. R. Maund, J. Shen, & M. H. Siegel ed., *Astronomical Society of the Pacific Conference Series Vol. 393, New Horizons in Astronomy*. pp 243+
 Ossenkopf V., Henning T., 1994, *A&A*, 291, 943
 Ostriker J., 1964, *ApJ*, 140, 1056
 Peretto N. et al., 2012, *A&A*, 541, A63
 Salpeter E. E., 1955, *ApJ*, 121, 161
 Sanhueza P., Garay G., Bronfman L., Mardones D., May J., Saito M., 2010, *ApJ*, 715, 18
 Sanhueza P., Jackson J. M., Foster J. B., Garay G., Silva A., Finn S. C., 2012, *ApJ*, 756, 60
 Sanhueza P., Jackson J. M., Foster J. B., Jimenez-Serra I., Dirienzo W. J., Pillai T., 2013, *ApJ*, 773, 123
 Schisano E. et al., 2014, *ApJ*, 791, 27
 Schuller F. et al., 2009, *A&A*, 504, 415
 Siringo G. et al., 2009, *A&A*, 497, 945
 Teixeira P. S., Lada C. J., Alves J. F., 2005, *ApJ*, 629, 276
 Tomisaka K., 1995, *ApJ*, 438, 226
 Wang K., Zhang Q., Wu Y., Zhang H., 2011, *ApJ*, 735, 64

Table 3. Parameter derived from molecular line observations. This table is an online only table that contains the velocity, peak temperature and line width and their errors for all the molecules detected in our sample. Here we show an extract of the table, showing the parameters of the N_2H^+ emission detected toward the clumps embedded in filament A.

Source	N_2H^+					
	v_{LSR} (km s^{-1})	δv_{LSR} (km s^{-1})	T_{A} (K)	δT_{A} (K)	Δv (km s^{-1})	$\delta \Delta v$ (km s^{-1})
A1	-35.40	0.19	0.22	0.04	2.38	0.44
A3	-36.85	0.03	1.49	0.04	2.39	0.06
A4	-36.06	0.09	0.60	0.04	2.88	0.18
A5	-39.90	0.21	0.17	0.02	3.27	0.40
A8	-37.19	0.05	0.77	0.03	2.44	0.10
A9	-37.53	0.07	0.71	0.05	2.36	0.17
A10	-38.10	0.06	0.88	0.04	2.49	0.13
A11	-37.79	0.09	0.43	0.04	2.50	0.20
A12	-38.39	0.06	0.56	0.04	2.11	0.15
A16	-39.35	0.19	0.34	0.04	3.44	0.39
A17	-39.65	0.05	0.86	0.04	2.28	0.11
A18	-35.45	0.09	0.80	0.03	3.96	0.16
A19	-37.59	0.04	1.14	0.03	3.19	0.08
A20	-38.52	0.03	1.19	0.03	2.75	0.07
A21	-39.70	0.03	1.92	0.05	2.53	0.07
A22	-39.70	0.03	1.68	0.04	2.66	0.06
A23	-38.79	0.06	0.85	0.03	3.41	0.11
A24	-40.13	0.03	2.12	0.04	3.12	0.06
A25	-38.96	0.05	1.34	0.04	3.52	0.09

Table 2. List of the molecular transitions observed as part of MALT90.

Molecule	Transition	Frequency (MHz)	n_{crit} (cm^{-3})	E_u/k (K)	Tracer
H ¹³ CO ⁺	J=1-0	86754.330	2×10^5	4.16	Column density
HN ¹³ C	J=1-0	87090.735	3×10^5	4.18	Column density
C ₂ H	N=1-0, J=3/2-1/2, F=2-1	87316.925	2×10^5	4.19	Density, Photodissociation tracer
HCN	J=1-0	88631.847	3×10^6	4.25	Density
HCO ⁺	J=1-0	89188.526	2×10^5	4.28	Density
HNC	J=1-0	90663.572	3×10^5	4.35	Density; cold chemistry
N ₂ H ⁺	J=1-0	93173.480	3×10^5	4.47	Density, cold chemistry
SiO	J=2-1	86847.010	2×10^6	6.25	Shock/outflow tracer
¹³ CS	J=2-1	92494.303	3×10^5	6.66	Column density
¹³ C ³⁴ S	J=2-1	90926.036	4×10^5	7.05	Column density
HNCO	$J_{K_a, K_b} = 4_0, 4^{-3}_0, 3$	88239.027	1×10^6	10.55	Hot core, shocks
CH ₃ CN	$J_K = 5_1 - 4_1$	91985.316	4×10^5	20.39	Hot core
HC ₃ N	J= 10-9	91199.796	5×10^5	24.01	Hot core
HC ¹³ CCN	J=10-9, F=9-8	90593.059	5×10^5	24.37	Hot core
HNCO	$J_{K_a, K_b} = 4_{1,3} - 3_{1,2}$	87925.238	1×10^6	53.86	Hot core, shocks
H	41 α	92034.475			Ionised gas

Table 4. Summary of the properties of the clumps embedded within the filaments. Column 1 and 2 list the IDs given to the clumps and their ATLASGAL name respectively. Column 3 lists the signatures detected in the infrared images. Column 4 lists the IR-based category assigned to each clump (for more details see section 4.1). Column 5 lists IRAS sources that are located within $30''$ from the clump. Column 6 lists the size of the clumps. Column 7 lists the assumed dust temperatures. Column 8 lists the mass derived from the dust emission. Column 9 lists the virial mass derived from the N_2H^+ line-width. Column 10 lists the ratio between the virial and dust mass and Column 10 lists the volume density.

Clump	ATLASGAL denomination	Infrared emission	Classification	IRAS	Size (pc)	Dust Temp. ^b (K)	M_{dust} (M_{\odot})	M_{vir} (M_{\odot})	α	$n(H_2)$ $\times 10^4$ (cm^{-3})
A1	AGAL339.054-00.412	24 μm emission	Proto-stellar	...	0.33	19	338	137	0.41	54.2
A2	AGAL338.937-00.422	4.5 μm -e, 24 μm -p ^c	Proto-stellar	...	0.32	19	194	34.1
A3	AGAL338.937-00.492	24 μm -p	Proto-stellar	...	0.81	19	742	339	0.46	8.1
A4	AGAL338.869-00.479	4.5 μm -e, 24 μm -p	Proto-stellar	...	0.54	19	261	327	1.25	9.6
A5	AGAL338.779-00.459	4.5 μm -e, 24 μm -p	Proto-stellar	...	0.36	19	132	281	2.14	16.3
A6	AGAL338.732-00.469	Dark	Pre-stellar	...	0.25	17	130	47.9
A7	AGAL338.551-00.419	4.5 μm -e, 24 μm -p	Proto-stellar	16396-4631	0.22	19	58	31.2
A8	AGAL338.424-00.411	4.5 μm -e, 24 μm -p	Proto-stellar	...	0.33	19	202	144	0.71	32.4
A9	AGAL338.394-00.406	4.5 μm -e, 24 μm -p	Proto-stellar	16390-4637	0.63	19	535	257	0.48	12.4
A10	AGAL338.327-00.409	4.5 μm -e, 24 μm -p	Proto-stellar	...	0.48	19	345	218	0.63	18.0
A11	AGAL338.199-00.464	Dark	Pre-stellar	...	0.26	17	117	119	1.01	38.5
A12	AGAL338.182-00.464	Dark	Pre-stellar	...	0.23	17	121	75	0.62	57.4
A13	AGAL338.112-00.464	Dark	Pre-stellar	...	0.33	17	254	40.9
A14	AGAL338.089-00.447	Dark	Pre-stellar	...	0.26	17	177	58.4
A15	AGAL338.026-00.476	Bright 8 and 24 μm	PDR	...	0.29	28	59	14.0
A16	AGAL337.994-00.514	Bright 8 and 24 μm	PDR	...	0.49	28	267	425	1.59	13.1
A17	AGAL337.974-00.519	Bright 8 and 24 μm	PDR	...	0.61	28	242	232	0.96	6.1
A18	AGAL337.939-00.532	Bright 8 and 24 μm	PDR	...	0.45	28	280	517	1.84	17.8
A19	AGAL337.931-00.521	Bright 8 and 24 μm	PDR	...	0.29	28	96	216	2.24	22.8
A20	AGAL337.934-00.507	Bright 8 and 24 μm	PDR	...	0.80	28	893	443	0.50	10.1
A21	AGAL337.889-00.489	Bright 8 and 24 μm	PDR	...	0.36	28	204	169	0.83	25.3
A22	AGAL337.891-00.491	Bright 8 and 24 μm	PDR	...	0.73	28	397	378	0.95	5.9
A23	AGAL337.916-00.477	Bright 8 and 24 μm	PDR	16374-4701	0.68	28	2462	579	0.24	45.2
A24	AGAL337.922-00.456	Bright 8 and 24 μm	PDR	...	1.16	28	2699	827	0.31	10.0
A25	AGAL337.927-00.432	Bright 8 and 24 μm	PDR	16373-4658	1.62	28	681	1479	2.16	0.9
B1	AGAL337.438-00.397	Bright 8 and 24 μm	HII Region	16352-4721	0.86	24	1221	415	0.34	11.1
B2	AGAL337.406-00.402	4.5 μm -e, and 24 μm -p	Proto-stellar	16340-4732	0.66	19	3673	526	0.14	73.8
B3	AGAL337.392-00.396	Bright 8 and 24 μm	HII Region	...	0.22	24	99	174	1.75	53.8
B4	AGAL337.382-00.394	Bright 8 and 24 μm	HII Region	...	0.28	24	167	138	0.82	44.0
B5	AGAL337.371-00.399	Bright 8 and 24 μm	HII Region	...	0.44	24	301	82	0.27	20.4
B6	AGAL337.216-00.391	Dark	Pre-stellar	...	0.29	17	353	83.5
B7	AGAL337.182-00.394	Dark	Pre-stellar	...	0.53	17	794	142	0.40	30.8
B8	AGAL337.152-00.394	4.5 μm -e, and 24 μm -p	Proto-stellar	16351-4722	1.13	19	2383	9.5
B9	AGAL337.139-00.382	4.5 μm -e	Proto-stellar	...	1.01	19	640	1084	0.46	3.6
B10	AGAL337.123-00.372	4.5 μm -e	Proto-stellar	...	0.77	19	503	644	1.00	6.4
B11	AGAL337.094-00.371	4.5 μm -e	Proto-stellar	16352-4721	0.45	19	313	19.8
B12	AGAL337.079-00.377	4.5 μm -e	Proto-stellar	...	0.48	19	495	25.8
C1	AGAL335.461-00.237	Dark	Pre-stellar	...	0.96	17	1203	490	0.41	7.8
C2	AGAL335.441-00.237	Dark	Pre-stellar	16264-4841	0.65	17	829	785	0.95	17.4
C3	AGAL335.427-00.241	4.5 μm -e, and 24 μm -p	Proto-stellar	...	0.80	19	1562	811	0.52	17.6
C4	AGAL335.402-00.241	24 μm -p	Proto-stellar	...	0.45	19	334	218	0.65	21.2
C5	AGAL335.337-00.282	Dark	Pre-stellar	...	0.35	17	410	55.2
C6	AGAL335.306-00.284	Dark	Pre-stellar	...	0.45	17	982	62.2
C7	AGAL335.304-00.332	Dark	Pre-stellar	...	0.82	17	1173	12.3
C8	AGAL335.292-00.379	24 μm -p	Proto-stellar	16263-4853	0.37	19	200	22.8
C9	AGAL335.289-00.281	Dark	Pre-stellar	...	0.26	17	322	105.6
C10	AGAL335.257-00.257	Dark	Pre-stellar	...	0.26	17	99	32.5
C11	AGAL335.249-00.304	Dark	Pre-stellar	...	1.12	17	2002	441	0.22	8.2
C12	AGAL335.236-00.322	Dark	Pre-stellar	...	0.33	17	179	125	0.70	28.7
C13	AGAL335.231-00.316	Dark	Pre-stellar	...	0.42	17	469	142	0.30	36.5
C14	AGAL335.221-00.344	Bright 8 and 24 μm	HII Region	...	0.87	24	771	447	0.58	6.8
C15	AGAL335.212-00.377	Dark	Pre-stellar	...	0.38	17	318	131	0.41	33.5
C16	AGAL335.197-00.389	Bright 8 and 24 μm	HII Region	16260-4858	0.52	24	278	11.4
C17	AGAL335.196-00.292	Bright 8 and 24 μm	HII Region	...	0.31	24	256	49.7
C18	AGAL335.162-00.384	Dark	Pre-stellar	...	0.23	17	177	84.0
C19	AGAL335.122-00.414	Dark	Pre-stellar	...	0.26	17	261	85.9
C20	AGAL335.099-00.429	Dark	Pre-stellar	...	0.44	17	603	40.9
C21	AGAL335.061-00.427	4.5 μm -e, and 24 μm -p	Proto-stellar	16256-4905	1.17	19	2277	792	0.35	8.2
C22	AGAL335.059-00.401	Dark	Pre-stellar	...	0.42	17	491	208	0.42	38.2

^b Assumed dust temperature based on the work of Guzman et al. (in press.).

^c 4.5 μm -e refers to extended 4.5 μm emission, and 24 μm -p refers to point like emission in this table.

Table 4 – *continued*

Clump	ATLASGAL denomination	Infrared emission	Classification	IRAS	Diam. [pc]	Dust Temp. [K]	m_{dust} [M_{\odot}]	m_{vir} [M_{\odot}]	α	n $\times 10^4$ [cm^{-3}]
D1	AGAL332.604-00.167	4.5 μm -e, 24 μm -p	Proto-stellar	16136-5038	0.96	19	1596	706	0.44	10.4
D2	AGAL332.559-00.147	Bright 8 and 24 μm	PDR	...	0.51	28	495	199	0.40	21.6
D3	AGAL332.544-00.124	Bright 8 and 24 μm	PDR	16132-5039	0.96	28	994	261	0.26	6.5
D4	AGAL332.531-00.159	Bright 8 and 24 μm	PDR	...	1.22	28	859	666	0.78	2.7
D5	AGAL332.519-00.114	Bright 8 and 24 μm	PDR	...	0.37	28	110	12.5
D6	AGAL332.506-00.119	Bright 8 and 24 μm	PDR	...	0.30	28	72	15.4
D7	AGAL332.496-00.121	Bright 8 and 24 μm	PDR	...	0.43	28	186	13.5
D8	AGAL332.469-00.131	Bright 8 and 24 μm	HII Region	...	0.56	24	399	190	0.47	13.1
D9	AGAL332.442-00.139	Dark	Pre-stellar	...	0.53	17	659	266	0.40	25.6
D10	AGAL332.412-00.156	Dark	Pre-stellar	...	0.34	17	230	33.7
D11	AGAL332.399-00.151	24 μm -p	Proto-stellar	...	0.40	19	228	50	0.22	20.5
D12	AGAL332.377-00.159	Dark	Pre-stellar	...	0.43	17	277	20.1
D13	AGAL332.352-00.116	Bright 8 and 24 μm	Proto-stellar	16122-5028	0.64	19	650	221	0.34	14.3
D14	AGAL332.332-00.122	8 μm point source	Proto-stellar	...	0.27	19	173	81	0.47	50.8
D15	AGAL332.296-00.094	Bright 8 and 24 μm	PDR	16119-5048	0.91	28	1304	511	0.39	10.0
D16	AGAL332.276-00.071	4.5 μm -e, and 24 μm -p	Proto-stellar	...	0.56	19	472	179	0.38	15.5
D17	AGAL332.254-00.056	Dark	Pre-stellar	...	0.98	17	612	416	0.68	3.8
D18	AGAL332.241-00.044	4.5 μm -e, and 24 μm -p	Proto-stellar	...	0.56	19	1646	502	0.31	54.1
D19	AGAL332.206-00.041	Dark	Pre-stellar	...	0.69	17	751	699	0.93	13.2
D20	AGAL332.204-00.024	Dark	Pre-stellar	...	0.50	17	334	155	0.93	15.4
D21	AGAL332.191-00.047	Dark	Pre-stellar	...	0.80	17	970	10.9
E1	AGAL332.467-00.522	4.5 μm -e, and 24 μm -p	Proto-stellar	16147-5100	0.86	19	1700	609	0.36	15.4
E2	AGAL332.411-00.471	8 and 24 μm emission	Proto-stellar	...	0.56	19	532	17.5
E3	AGAL332.409-00.504	Bright 8 and 24 μm	PDR	16143-5101	0.81	28	484	416	0.86	5.3
E4	AGAL332.394-00.507	24 μm -p	Proto-stellar	...	0.29	19	109	69	0.63	25.7
E5	AGAL332.351-00.436	Bright 8 and 24 μm	HII Region	16137-5100	0.88	24	798	311	0.39	6.8
E6	AGAL332.336-00.574	Bright 8 and 24 μm	PDR	...	0.70	28	452	141	0.31	7.6
E7	AGAL332.334-00.436	Dark	Pre-stellar	...	0.34	17	451	105	0.23	66.2
E8	AGAL332.326-00.454	Dark	Pre-stellar	...	0.65	17	697	134	0.19	14.6
E9	AGAL332.322-00.552	Bright 8 and 24 μm	PDR	...	0.39	28	264	117	0.44	25.7
E10	AGAL332.312-00.556	Diffuse 8 and 24 μm emission	PDR	16141-5107	0.83	28	660	476	0.72	6.7
E11	AGAL332.281-00.547	4.5 μm -e, and 24 μm -p	Proto-stellar	...	0.77	19	1251	497	0.40	15.8
E12	AGAL332.252-00.539	Diffuse 8 and 24 μm emission	PDR	...	0.50	28	375	97	0.26	17.3
E13	AGAL332.226-00.536	4.5 μm -e, and 24 μm -p	Proto-stellar	...	0.83	19	1096	344	0.31	11.1
E14	AGAL332.156-00.449	Bright 8 and 24 μm	HII Region	16128-5109	0.93	24	2557	1057	0.41	18.3
E15	AGAL332.147-00.439	Bright 8 and 24 μm	PDR	...	0.27	28	240	329	1.36	70.5
E16	AGAL332.144-00.469	Bright 8 and 24 μm	PDR	...	0.86	28	464	4.2
E17	AGAL332.142-00.436	Bright 8 and 24 μm	PDR	...	0.57	28	353	879	2.49	11.0
E18	AGAL332.141-00.466	Bright 8 and 24 μm	PDR	...	0.59	28	405	821	2.02	11.4
E19	AGAL332.141-00.446	Bright 8 and 24 μm	PDR	...	0.70	28	813	1736	2.14	13.7
E20	AGAL332.134-00.422	Bright 8 and 24 μm	PDR	...	0.72	28	376	5.8
E21	AGAL332.094-00.421	Bright 8 and 24 μm	HII Region	16124-5110	0.81	24	1960	491	0.25	21.3